TECHNICAL ARTICLE

Study of Microstructure, Mechanical Properties, and Corrosion Behavior of As-Cast Ni-Ti and Ti-6Al-4V Alloys

Ramadan N. Elshaer and Khaled M. Ibrahim

Ni-Ti and Ti-6Al-4V alloys were cast as ingots using vacuum arc remelting furnace. The microstructure of as-cast Ni-Ti alloy consists of NiTi matrix as well as Ti$_2$Ni dendrites. As-cast Ti-6Al-4V alloy revealed a structure composed of equiaxed β grains and varied α-phase morphologies. Ti-6Al-4V alloy registered maximum ultimate compressive strength of 2042 MPa, and also reported large reduction in height (18%). However, Ni-Ti alloy showed minimum ultimate compressive strength of 1804 MPa and low reduction in height (3%). The wear rate of both as-cast Ni-Ti and Ti-6Al-4V alloys significantly increased with saline solution (0.9% NaCl) condition compared to the dry testing condition. Saline solution harmed the wear resistance by about 2-4 times compared to the dry conditions. The corrosion rate of Ti-6Al-4V in saline solution (0.9% NaCl) was 0.000171 mm/yr which is almost half the value of Ni-Ti alloy (0.00038 mm/yr).

1. Introduction

Material scientists choose Ni-Ti shape memory alloys (SMAs) based on close or similar atomic ratios because of their distinct shape memory properties, outstanding superelasticity, good mechanical properties, wear, as well as corrosion resistance (Ref 1-4). Ni-Ti-based alloys have become increasingly popular in biomedicine, aircraft, solid-state cooling, and microelectromechanical systems in recent years due to their superior properties (Ref 1-6). They are mostly employed including orthodontic material, medical equipment, hard tissue as well as soft tissue implants in the biomedical alloys field (Ref 2, 6). In microelectromechanical systems, Ni-Ti-based alloys are utilized to make functioning microgrippers, micromirror actuators as well as fluid-flow valves (Ref 7, 8). Also, Ni-Ti- alloys are mostly utilized as cryogenic fittings in military aircraft hydraulic systems, in addition to helicopter blade trajectory controls in aeronautical and space technologies (Ref 5). Ni-Ti alloys have a shape memory effect and excellent mechanical properties primarily as a result of martensitic thermoelastic transition and stress, which is the inverse process or temperature-induced conversion between high-temperature symmetric austenite phase (B2) as well as symmetric martensitic phase (B19′) at low temperatures (Ref 9).

Because of its advantages, including resistance to body fluid effects, high strength-to-weight ratio, and superior corrosion/ oxidation resistance, titanium alloys are appealing choices for aerospace, automotive, petroleum, and biomedical industries. Due to its excellent overall properties, such as high specific strength, exceptional corrosion resistance, magnetic resistance as well as good elevated temperature performance, Ti-6Al-4V is the most widely used Ti alloy in aerospace, automotive and orthodontic applications (Ref 10-12). Ingot metallurgy is often used to make Ti-6Al-4V alloy, which has lamellar structure as-cast ingots (Ref 13). The lamellar microstructure is a common Ti-6Al-4V alloy microstructure, with moderate strength, and excellent fatigue cracks growth resistance. However, ductility is extremely low (Ref 14).

Because titanium is a very reactive metal in the molten state, it should be melted and poured in a vacuum to yield quality casting. Most nickel and titanium cast parts are melted using vacuum arc remelting (VAR), vacuum induction skull melting (ISM) as well as electron beam melting (EBM) techniques which include consumable arc melting as well as nonconsumable arc melting (Ref 15). ISM aids in the chemical composition homogeneity of Ni-Ti; however, it necessitates the use of a graphite crucible which results in Ti and C reaction. During melting and solidification, titanium carbide (TiC) forms in Ni-Ti, increasing Ni content of the alloy matrix and decreasing martensite transformation temperature (Ref 16, 17). VAR does not require a graphite crucible; here, there is less crucible contamination in Ni-Ti. However, it usually results in less uniform chemical composition of Ni-Ti ingots, necessitating multiple remelting (Ref 18, 19). Casting of nickel and titanium alloys are often cost-effective and competitive compared with machining, forging, and other establishing manufacturing techniques. Increasing casting process in manufacturing some parts in aerospace structures could significantly reduce the cost. Therefore, casting of Ni-Ti, as well as titanium alloys, may be considered a classic near net shape process. However, strength and ductility disadvantages must be accepted when compared to forged parts. These can at least be partly compensated by intelligent casting-specific component

Ramadan N. Elshaer, Tabbin Institute for Metallurgical Studies, Cairo, Egypt; and **Khaled M. Ibrahim**, Central Metallurgical R&D Institute, Cairo, Egypt. Contact e-mail: ramadan_elshaer@yahoo.com.

design. Cast alloys Ni-Ti and Ti-6Al-4V have an irregular microstructure, which has an impact on the alloys' mechanical properties. Ti-6Al-4V alloy in the cast condition can be used in different applications, such as automotive and motorcycle; connecting rod, intake valve, outlet valve, and rim screws, some in implant applications. NiTi alloy has also many applications in the cast condition, such as staple implants, Belleville springs, meshes, helical springs, screws, and hexagonal honeycombs.

The microstructures also mechanical properties of cast Ni-Ti and Ti-6Al-4V were studied by several researchers, which laid the groundwork for the following heat treatment processing of cast Ni-Ti and Ti-6Al-4V. Wen et al. (Ref 20) found that Ni-Ti alloy can be enhanced strength with nearly little ductility loss, resulting in the sample having the optimum strength-ductility synergy that was annealed at 400 °C for 20 min. This is owing to the recovered nanostructure, which has a modest dislocation density and outstanding strengthening and strain hardening properties. Frenzel et al. (Ref 21) reported that increased Ni content in Ni-Ti alloy lowers phase-change temperatures, thermal hysteresis width as well as the heat of transformation. As a result, the rigorous restriction during melting by carefully managing the Ni to Ti ratio to fulfill the acceptable tolerance in the transition temperatures is critical to the effective application of Ni-Ti alloy to engineering areas (Ref 22). Seo et al. (Ref 23) reported that during solution treatment, Ti-6Al-4V alloy cooled quickly, in which the hardness will increased. This is of course attributed to the development of thinner α plates and/or a larger α' fraction. Because of Ti_3Al precipitation in α and/or fine α plates from α', regardless of cooling conditions, hardness increased even more during aging. Liu et al. (Ref 24) described Ti-6Al-4V with high strength, outstanding ductility, and good fatigue properties. In a previous study by Elshaer and Ibrahim (Ref 25), applying 15% cold deformation on TC21 Ti alloy exhibited an elongated thin β-phase embedded in α-phase.

Ni-Ti and Ti-6Al-4V alloys are considered biomedical materials. Both alloys can be used in orthodontic applications. Hence, it is important to characterize both alloys firstly in the as-cast condition, where it is hard to find such a study. Therefore, this research work aims at studying the behavior of those alloys in the as-cast condition. It is hard to find previous work gathering these two alloys, especially in the cast condition. This research also offers a guideline for these alloys in the as-cast condition as well as microstructure, mechanical properties, and corrosion resistance are concerned when using these alloys in orthodontic applications.

2. Experimental Procedures

The following elements: pure titanium (Ti), nickel (Ni), aluminum (Al), and vanadium (V), with high purity of 99.9% were used for preparing the cast ingots. Ni-Ti and Ti-6Al-4V alloys were firstly cast as ingots using a vacuum arc remelting furnace. Actually, we used the vacuum arc melting technique for casting our samples, where an electrode was used for melting the raw material of the used alloys. In such case, the material was melted in the copper mold inside the vacuum chamber and take the shape of the copper mold as a disk with a diameter of approx. 80 mm and a thickness of 12 mm. The melting point of Ti-6Al-4V alloy reached 1700 °C and Ni-Ti alloy reached 1400 °C during casting process and just before

solidification inside the copper mold. After finishing the melting process under a vacuum, electromagnetic stirring was applied to homogenize the liquid metal and improve the quality of the cast alloys. Hence, both studied alloys were cast with very high quality without any defects inside. Figure 1 shows the arc and sample positions in the vacuum arc remelting furnace. The chemical compositions of the studied as-cast alloys were $Ni_{48}Ti_{52}$ and $Ti_{90}Al_6V_4$ using a Foundry Pro-master spectrometer (OXFORD device, Germany). For both studied alloys, 150 gm of raw materials was placed in a water-cooled copper crucible. The cast ingots were remelted six times to assure chemical composition homogeneity under a high vacuum that reached 1×10^{-5} mbar. The average chemical compositions of Ni-Ti and Ti-6Al-4V alloys are listed in Table 1. The cast ingots (disk shape $\Phi80 \times 12$ mm), Fig. 2, were cut using wire-cutting technology and a fine cutter machine for investigations (Leco LX31 Optical Microscope (OM), x-Ray Diffraction (XRD) Panalytical/model X'Pert PRO with a diffractometer using Cu Kα1 radiation in a 2θ range of 10°-100° and recording data at 0.02° with steps at a speed of 0.004°/min as well as field emission scanning electron microscope (FESEM) Quanta-FEI/FEG-250 Netherland with Energy Dispersive x-Ray analysis (EDX), and mechanical testing (hardness, compression, wear, and corrosion). For optical metallographic examination, samples were polished using SiC emery sheets with a granularity of up to 1500 before being polished with Al_2O_3. The polished Ni-Ti sample was etched with a solution consisting of 10% HF, 45% HNO_3, 45% H_2O and 2% HF, 6% HNO_3, 92% H_2O for Ti-6Al-4V sample. Inverted OM and FESEM were used for examining the microstructure of etched samples. For determining the existing
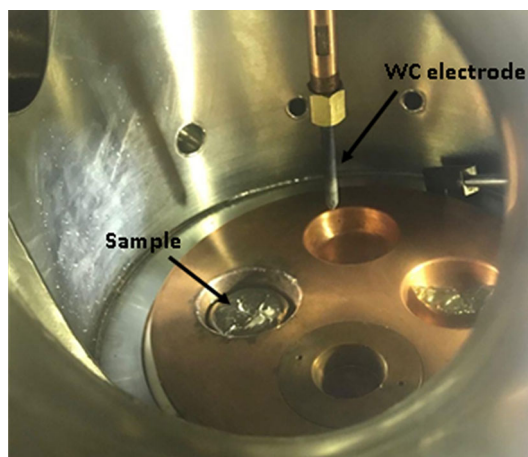

Fig. 1 WC electrode and sample positions in the vacuum arc melting furnace

Table 1   Chemical compositions of studied as-cast Ni-Ti and Ti-6Al-4V alloys, wt.%

Alloy	Average chemical composition, wt.%							
	Ti	**Ni**	**Al**	**V**	**Si**	**Fe**	**Sn**	**Zn**
Ni-Ti	51.8	47.5	…	…	0.32	0.38	0.02	0.03
Ti-6Al-4V	90.16	0.001	5.54	3.76	0.03	0.31	0.20	…

Fig. 2 Shape of alloy ingots (disk shape $\Phi 80 \times 10$ mm)
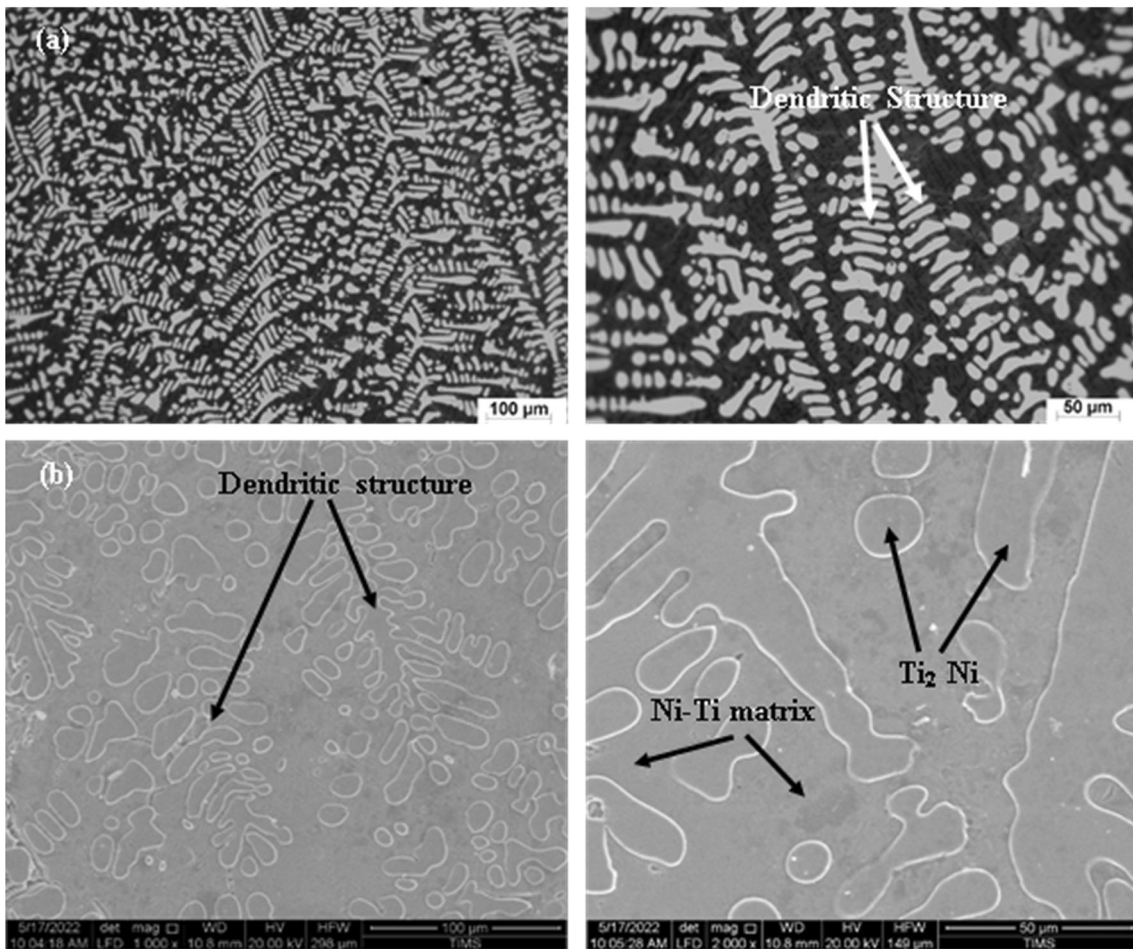

Fig. 3 Microstructure of Ni-Ti alloy (a) OM and (b) FESEM
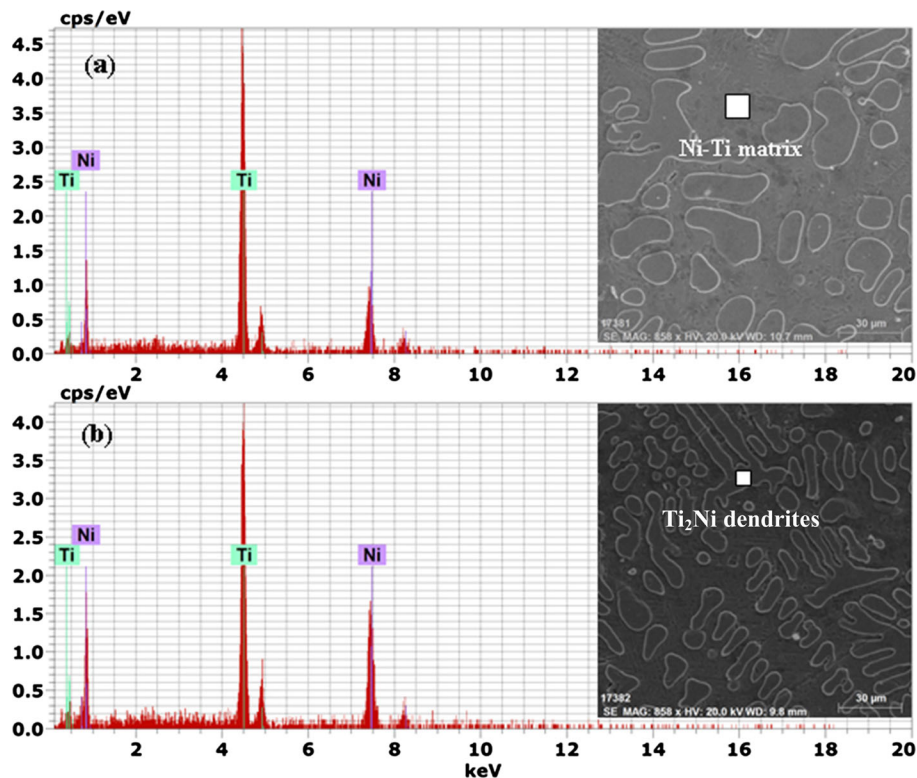
Fig. 4 EDX analysis of Ni-Ti alloy for NiTi matrix (a) and Ti_2Ni dendrites (b)

phases in each alloy, XRD examination was performed on polished samples as well as EDX to identify the phase's content.

Vickers hardness test was carried out using Vickers hardness tester apparatus (model 5030 SKV, England) in accordance with ASTM E92-16 standard, using 10 kg force and 15 s dwell time. For calculating the average hardness of each sample, five readings were taken. Rectangular samples ($8 \times 8 \times 10$ mm) were prepared for compression testing according to ASTM E9-16 standard. The compression test was carried out at ambient temperature with a crosshead speed of 1 mm/min using a universal testing machine (UH-F1000 KNI, Japan). For each alloy, three samples were measured and the average compressive value was taken. Reduction of height was measured using the following equation: $[R_h = ((h_b - h_a)/h_a)*100]$, where R_h reduction of height, h_b height of sample before testing, and h_a height of sample after testing. Pin-on-ring tribometer testing machine was used for conducting wear test according to ASTM G99-17. Wear testing was conducted at ambient temperature for both dry and wet (saline solution, 0.9% NaCl) conditions. The wear sample with a rectangular form of $8 \times 8 \times 10$ mm was pushed against a rotating stainless-steel ring at a speed of 1 m/s. The wear test was applied for 15 min and different applied loads of 70, 90, 100, and 120 N. Three samples were carried out at each load, and the average readings were collected. The samples were weighed using an electronic scale with 0.1 mg accuracy before and after the wear test. Weight loss was used to evaluate the test results. FESEM was used to examine the fracture surface following compression testing, as well as worn surfaces of some selected samples.

Ni-Ti and Ti-6Al-4V samples were also corrosion tested using potentiodynamic polarization and electrochemical impedance (EIS) techniques. The samples were polished to 1500-grit, ultrasonically cleaned, ethanol rinsed, and then dried. For each condition, the experiment was measured three times. A Pt counter electrode was employed in a standard three-electrode cell in a cylindrical glass cell with a single chamber. All potentials were measured at 25 °C with reference to a saturated calomel electrode (SCE). Analytical-grade chemicals, as well as bi-distilled water, were used for preparing a sodium chloride medium. Computerized Potentiostat/Galvanostat was used for measuring potentiodynamic polarization (Autolab PG STAT 30). Starting at -0.3 V below E_{corr} and moving upwards to 1 V above E_{corr}, potential was scanned. Using AutoLab software, corrosion parameters such as corrosion current (I_{corr}), corrosion potential (E_{corr}), as well as corrosion rate (CR) were calculated from polarization curves. EIS tests were employed using Autolab instrument. At room temperature, EIS measurements were made at open circuit potential with 10 mV amplitude voltage signal spanning a frequency range of 1 Hz to 65 kHz. EIS curves were analyzed, using the Fit and Simulate property in the AutoLab software for deducing the impedance parameters: dispersion factor (n), as well as solution resistance (Rs), polarization resistance (R_p), and double-layer capacitance (Cdl).

3. Results and Discussion

3.1 Microstructure Evaluation of As-Cast Ni-Ti and Ti-6Al-4V Alloys

Figure 3 shows the microstructure of the investigated as-cast Ni-Ti alloy. The microstructure of as-cast Ni-Ti alloy was mostly composed of inhomogeneous dendritic structure, Fig. 3(a). Dendritic microstructural begins to expand out in
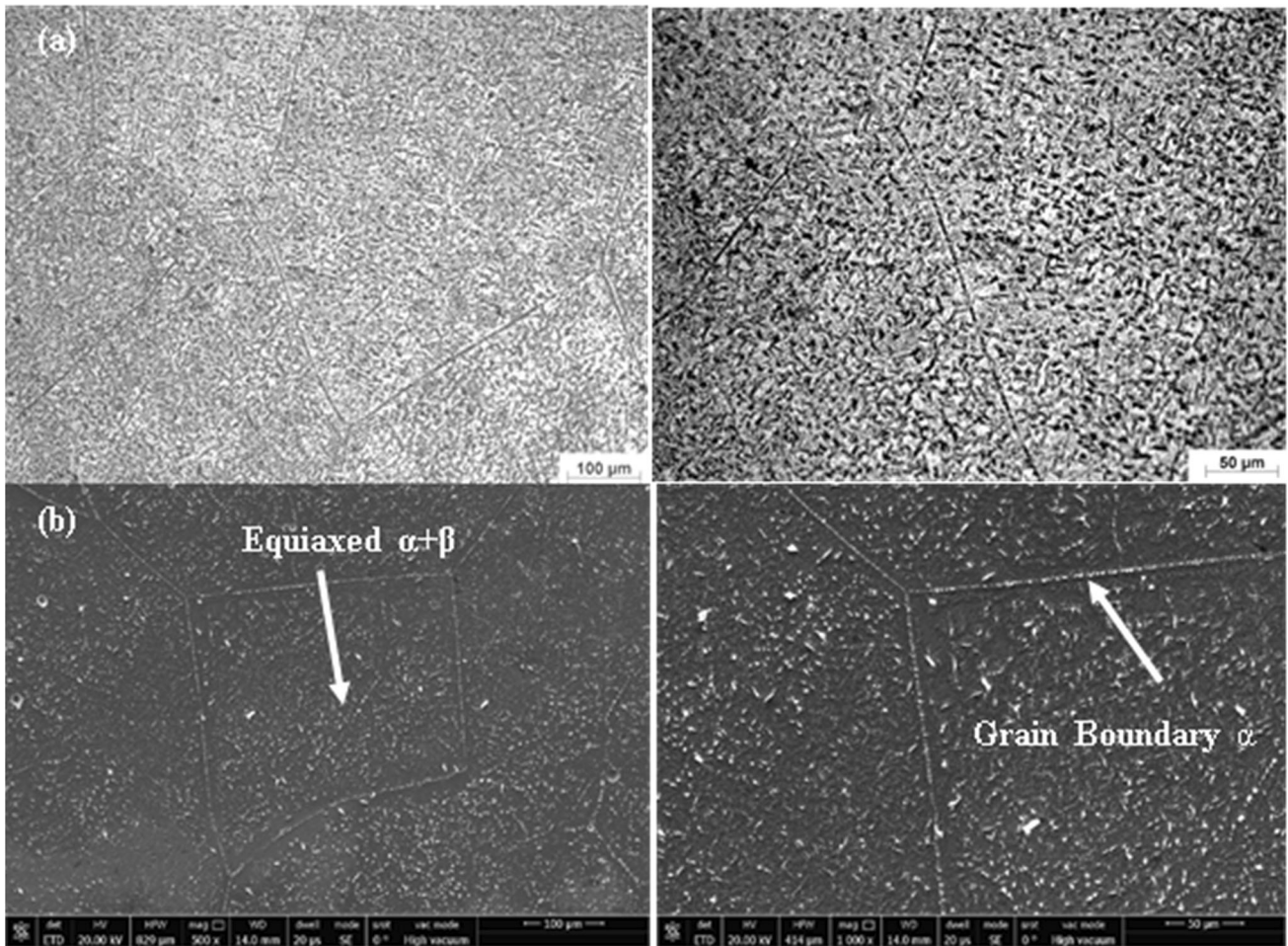
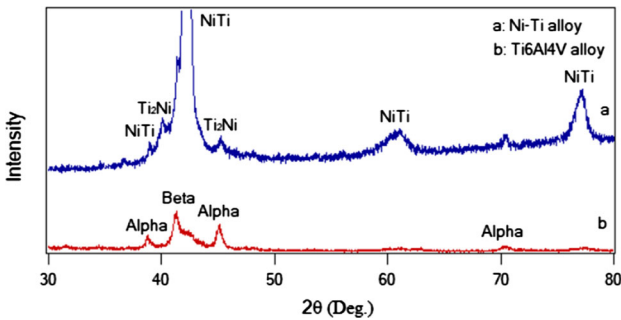**Fig. 5** Microstructure of Ti-6Al-4V alloy (a) OM and (b) FESEM

Fig. 6 XRD pattern of (a) Ni-Ti and (b) Ti-6Al-4V alloys. *Reference codes for each detected phase: 01-076-8564 (NiTi), 00-018-0898 (Ti₂Ni), 01-089-2762 (Alpha), and 01-089-4913 (Beta)

Fig. 7 Hardness of the investigated cast Ni-Ti and Ti-6Al-4V alloys

the same direction as cooling, whereas orientated randomly in OM images, and there is no distinct crack or porosity (Ref [26]). According to the phase diagram, Ni-Ti shape memory alloy near the equiatomic ratio refers to the β phase at a high temperature, which has a BCC crystal structure (Ref 27). As shown in Fig. 3(b), the microstructure consists of NiTi matrix and Ti_2Ni phase (dendritic structure) which are forming as inhomogeneous dendrite structure. The existing phases in the NiTi sample were analyzed using EDX, Fig. 4. Three different areas were chosen for each phase to ensure homogeneity of phases and the average was taken. Ni (47%) and Ti (53%) were
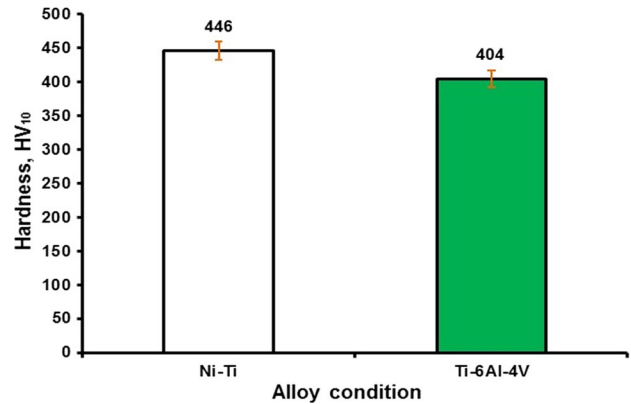
found in the matrix. However, Ni (37%) and Ti (63%) were presented in Ti_2Ni.

On the other hand, as-cast Ti-6Al-4V alloy showed equiaxed prior β grains in which α was precipitated (Ref 28), as shown in Fig. 5. The α-phase has a hexagonal closed-packed (HCP) crystal structure at ambient temperature, while β-phase has BCC structure. The α-phase normally formed as layers at the grain boundaries and particles in the matrix. The β-phase is formed as lathes in the matrix (Ref 29). Because the alloy is in the as-cast condition, the structure can be described as an
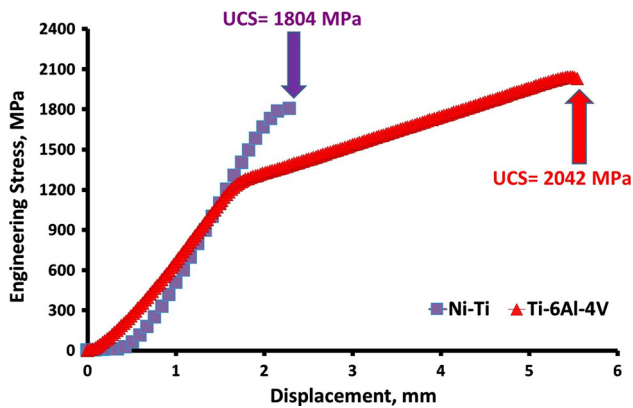
Fig. 8 Engineering stress–displacement curves of cast Ni-Ti and Ti-6Al-4V alloys

Table 2 Compressive properties and hardness for as-cast Ni-Ti and Ti-6Al-4V alloys

Alloy	Yield compressive strength, MPa	Ultimate compressive strength, MPa	Reduction in height, %	Hardness, HV_{10}
Ni-Ti	1730	1804	5	446
Ti-6Al-4V	1250	2042	18	404

inhomogeneous structure. As shown in Fig. 5(b), the grains size is variant ranging from 350 to 550 μm. According to Damisih et al. (Ref 30), as-cast Ti-6Al-4V alloy microstructure revealed a structure composed of equiaxed β grains and varied α-phase morphologies. Figure 6 shows XRD patterns of the studied as-cast Ni-Ti and Ti-6Al-4V samples. The patterns for Ni-Ti alloy verified the phases existing in the microstructure, including Ni-Ti matrix (hexagonal structure) and Ti_2Ni dendrites (cubic structure). And Ti-6Al-4V alloy has also confirmed the existence of α (HCP) and β (BCC) phases in the microstructure.

3.2 Hardness of Cast Ni-Ti and Ti-6Al-4V Alloys

Figure 7 illustrates hardness values of as-cast Ni-Ti and Ti-6Al-4V alloys. The highest hardness of 446 HV_{10} was reported for Ni-Ti alloy due to Ti_2Ni dendrites existing in the Ni-Ti matrix. The lowest hardness (404 HV_{10}) was recorded for Ti-6Al-4V alloy because of the coarse β-grains as well as the presence of inhomogeneous $\alpha + \beta$ structure. There is also an increase in hardness of approximately 10% for Ni-Ti alloy compared to Ti-6Al-4V alloy. Previous studies carried out by Ibrahim et al. (Ref 28) and by Singh et al. (Ref 31) have also confirmed these results. In our work, the hardness of Ti-6Al-4V alloy reached to 404 HV_{10} because we used vacuum arc melting technique where the molten metal is solidified in coiled copper mold. However, in reference (Ref 28), the samples were poured into a graphite mold, and therefore the hardness (350 HV_{10}) is lower than ours due to the solidification rate between them.

3.3 Compression Properties

Figure 8 presents the engineering stress–displacement curve of both cast Ni-Ti and Ti-6Al-4V alloys. Ti-6Al-4V alloy gave maximum ultimate compressive strength (UCS) of 2042 MPa, and it reported as well the largest reduction in height (18%). On the other hand, Ni-Ti alloy showed the minimum ultimate compressive strength of 1804 MPa, and the smallest reduction in height (3%) because of forming Ti_2Ni dendrites inside Ni-Ti matrix. During the compressive test, Ti_2Ni produced embrittlement and crack initiation, which in turn decreased the strength of Ni-Ti alloy as compared to Ti-6Al-4V. The difference between ultimate and yield compressive strengths is significantly clear in Fig. 8. For Ti-6Al-4V alloy, yield compressive strength was 1250 MPa owing to the presence of a

large amount of α-phase that enhanced the compressive deformation. For Ni-Ti alloy, the difference between the values of ultimate and yield compressive strengths is very low where yield strength was 1730 MPa. In a previous study on Ti-6.55Al-3.41Mo-1.77Zr alloy by Ibrahim et al. (Ref 32), it was noted also that the difference between the values of yield and ultimate compressive strengths is significantly clear. This finding was matched with the current study's results.

For as-cast Ni_{48}-Ti_{52} alloy, the austenite B2 phase can be converted to the martensite phase with increasing stress, resulting in a martensite transition peak in stress–strain curves (Ref 33). Because the matrix phase of Ni-Ti alloy has a body-centered cubic structure and does not contain B2 phase with large grain sizes, there is no martensite transition peak that can be discovered at the nominal stress-displacement curve shown in Fig. 8. According to Sun et al. (Ref 34-36), as the particle size of B2 phase decreases, the strain of martensite transition peak decreases. When the particle size approaches 10 nm, the martensite transition peak almost vanishes, i.e., the stress–strain curve demonstrates a smooth phase transition caused by stress. Li et al. (Ref 37) reported that $Ti_{48.5}Ni_{51}Fe_{0.5}$, as well as $Ti_{48}Ni_{51}Fe_1$ alloys, exhibited high yield and fracture strengths which can be employed as engineering materials with outstanding mechanical properties. Moreover, $Ti_{48.5}Ni_{51}Fe_{0.5}$ alloy is a suitable biomedical alloy for hard tissue implants due to its low elastic modulus as well as high elastic energy. Further details of compressive properties and hardness for as-cast Ni-Ti and Ti-6Al-4V alloys are listed in Table 2. It is clear from Table 2 that Ti-6Al-4V alloy has better compressive properties than Ni-Ti alloy. However, Ni-Ti alloy has higher hardness than Ti-6Al-4V alloy.

3.3.1 Fracture Behavior of Compressive Samples. The fracture surface after compression test at ambient temperature for as-cast Ni-Ti and Ti-6Al-4V samples is seen in Fig. 9. As-cast Ni-Ti sample's fracture surface displays a river pattern with cleavage plane as well as tear ridge, indicating that it is a cleavage fracture, Fig. 9(a). The fracture features are matched with the obtained result of the compressive stress–displacement curve and the low reduction in height (3%). On the other hand, the as-cast Ti-6Al-4V sample revealed medium dimple regions on a quasi-cleavage fine fracture surface, Fig. 9(b), which pointed out the high ductility (18% reduction in height).

3.4 Wear Properties

The correlation between wear rate at different applied loads of 70, 90, 100, and 120 N for the investigated alloys at dry and wet (0.9% NaCl) conditions is presented in Fig. 10. Molinari et al. (Ref 38) proposed that titanium alloys have bad tribological properties due to two main reasons: (1) low plastic shearing resistance as well as low work-hardening, and (2) surface oxide provides just a limited amount of protection
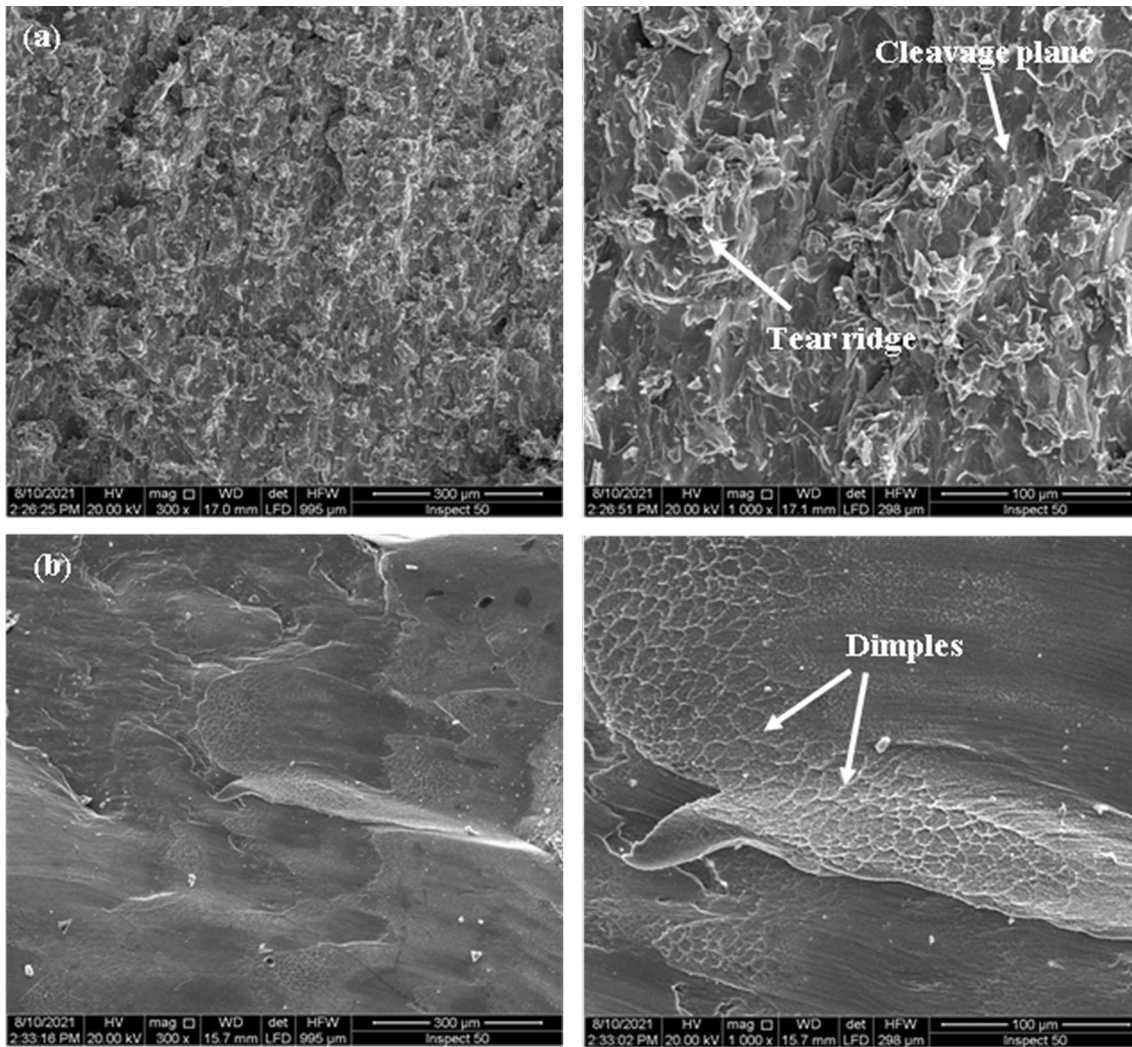
Fig. 9 Fractography of compressive samples (a) Ni-Ti, (b) Ti-6Al-4V
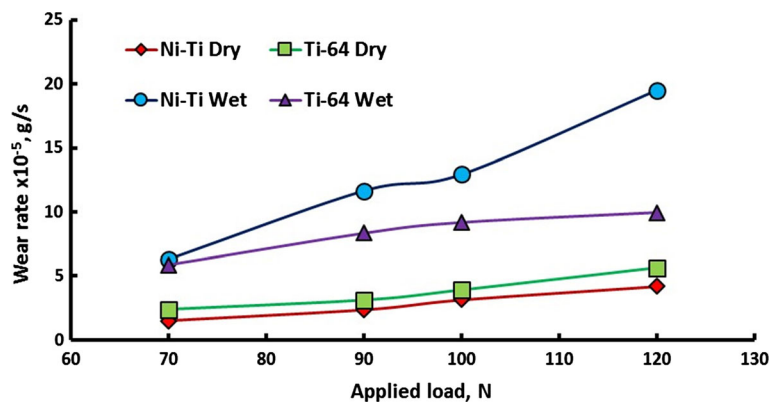

Fig. 10 Wear rate of cast Ni-Ti and Ti-6Al-4V alloys in both dry as well as wet environments

because of high flash temperature caused by friction during wear process. Temperature, material hardness, toughness, and strength, as well as crystal structure compatibilities, are the main factors influencing wear performance (Ref 39). For Ni-Ti alloy, however, exhibited some variances (Ref 40, 41). Shape memory is a unique effect as well as superior superelasticity of NiTi alloys, which have been found to play a significant role in Ni-Ti wear performance (Ref 21, 42-46).

Both as-cast Ni-Ti and Ti-6Al-4V alloys exhibited the same wear pattern, in which wear rate increased with increasing applied load, Fig. 10. This occurs as the applied load increases, causing higher shear stress over the contact surfaces. The wear
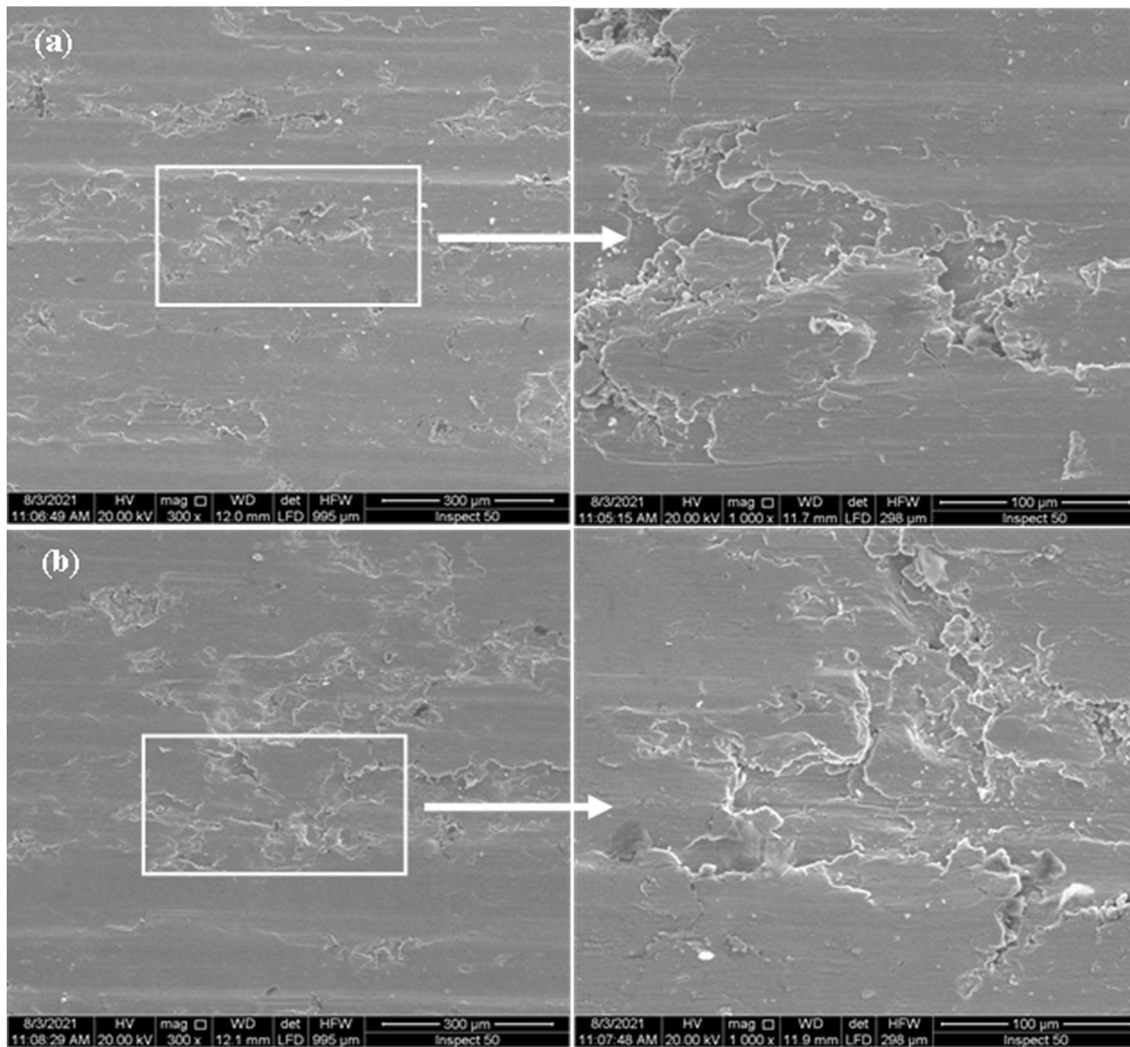
Fig. 11 Worn surfaces of Ni-Ti alloy at a load of (a) 100, and (b) 120 N

rate was found in a stable state at all applied loads under dry and wet conditions excepting the applied load of 120 N for as-cast Ni-Ti alloy under wet condition (0.9% NaCl), where there was a sharp increase in wear rate. The wear resistance is, of course, linked to microscopic structure of the material and its hardness. The wet condition showed higher wear rate as compared to the dry one. It is found that the wet condition harmed the wear resistance by about 2-4 times as compared to the dry condition. This is owing to the oxide film that formed over the sample surfaces. Titanium reacts aggressively with oxygen when exposed to saline solution, forming either crystalline or non-crystalline oxide film. As seen in Fig. 10, minimum wear rate was reported for Ni-Ti alloy of 4.2×10^{-5} g/s at 120 N under dry sliding conditions due to its high hardness. For Ti-6Al-4V, this value was 5.63×10^{-5} g/s at the same load. The existing phases in as-cast structure of Ni-Ti alloy (NiTi matrix and Ti_2Ni dendrites) will resist well against the counterpart. In such case, the soft NiTi matrix is protected well from the hard phases existing in the microstructure against the rotating ring. This means Ti_2Ni dendrites will shield the surface from adhesion and strengthening the matrix against wear. However, the soft α-phase existing in as-cast Ti-6Al-4V alloy showed a slightly increased

wear rate compared to as-cast Ni-Ti in dry condition at all ranges of the applied load. Ohidul Alam and Haseeb (Ref 47) showed that high-alloyed titanium alloys had better wear resistance than low-alloyed ones during dry sliding. This may be due to titanium's superior plastic deformation resistance (greater hardness), spalling resistance as well as plastic shearing resistance (Ref 47). Wen et al. (Ref 21) studied also the wear resistance of nanostructured Ni-Ti alloy, which obtained an improvement in wear behavior. This is mostly owing to the high residue martensite content, which allows greater elastic deformation, lower friction temperatures, and increased resistance. However, the wear rate of as-cast Ni-Ti and Ti-6Al-4V alloys significantly increased under wet (0.9 NaCl) conditions compared to dry conditions, particularly for Ni-Ti alloy at 120 N. According to the obtained wear rate results, Ni-Ti alloy had the worst wear resistance in saline solution than the Ti-6Al-4V. For wet condition, saline solution made an oxide film on the sliding surface, which in turn will increase the wear rate. It is proposed that in wet condition, the wear rate is higher due to fragmentation of the formed oxide layer over the sample surface and occurring three-body wear mechanism as compared to two-body wear mechanism in dry condition.
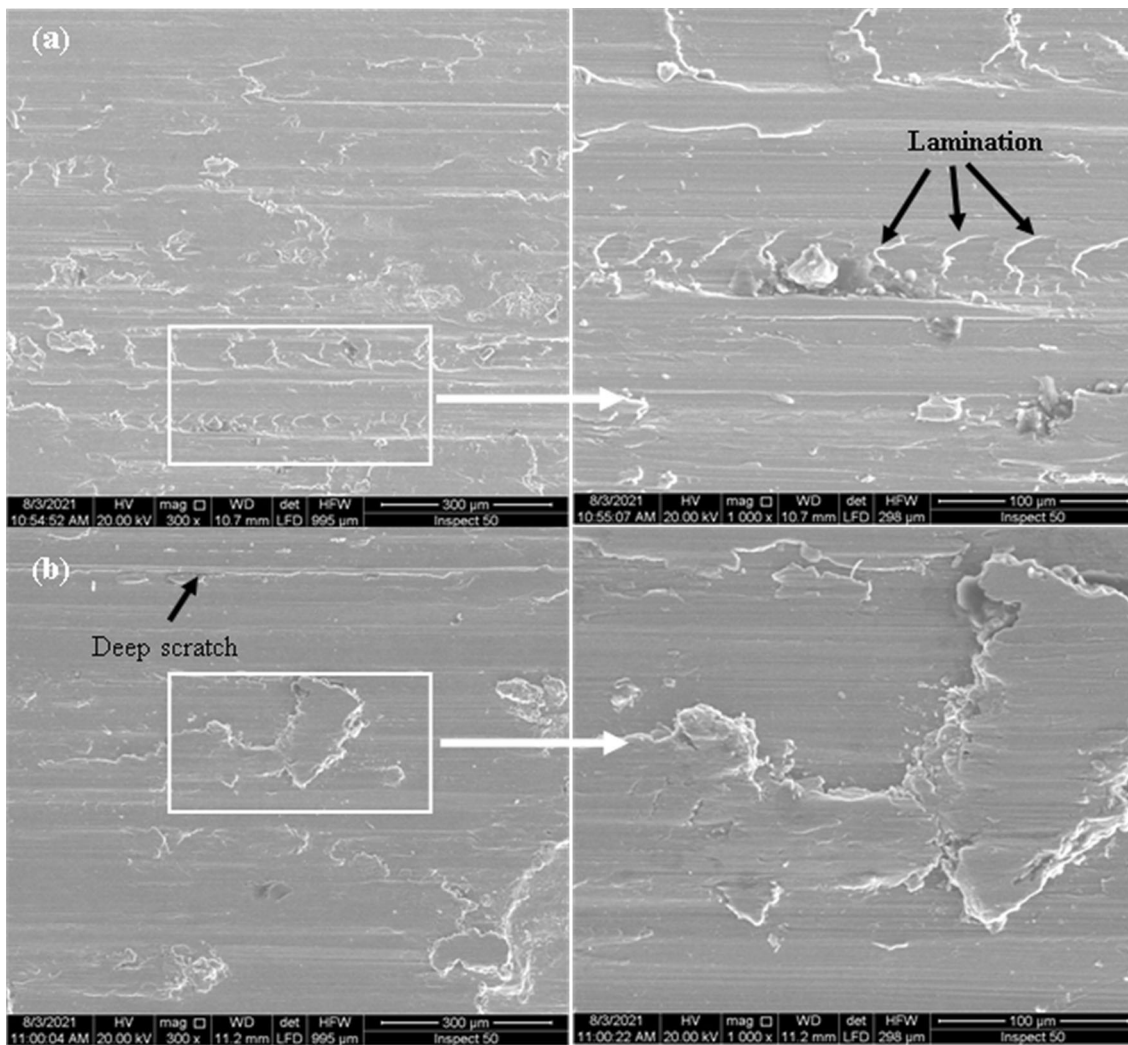
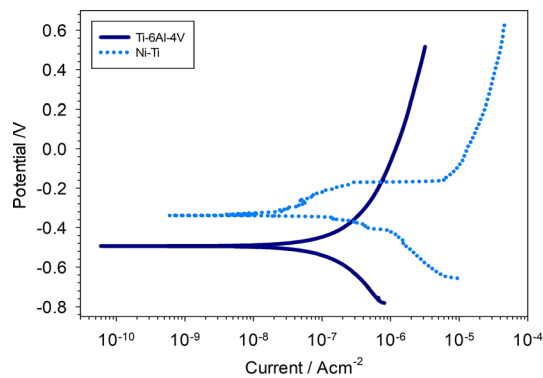**Fig. 12** Worn surfaces of Ti-6Al-4V alloy at the load of (a) 100, and (b) 120 N

Fig. 13 Potentiodynamic polarization curves of tested alloys in saline solution

3.4.1 Worn Surface of Samples. The four types of mechanisms that cause materials to wear failure are adhesive point shear, impact, microscopic cutting, and fatigue (Ref 42, 48). Worn surface morphologies of as-cast Ni-Ti and Ti-6Al-4V alloys in dry conditions at applied loads of 100 and 120 N are shown in Figs. 11 and 12. For as-cast Ni-Ti alloy, the worn surface was flat and smooth, with a few small scratches at the applied load of 100 N, as shown by the arrows in Fig. 11(a). At an applied load of 120 N, the worn surface showed a lamination wear mechanism with deep grooves over the worn surface, as indicated by the arrows in Fig. 11(b).

When Ti-6Al-4V alloy slides against the counterface, several wear mechanisms have been documented, including delamination, oxidation, and adhesion wear (Ref 47). For as-cast Ti-6Al-4V alloy at an applied load of 100 N, arrows and area in Fig. 12(a), illustrate that the worn surface showed many wear mechanisms. These observed mechanisms are lamination and micro-cutting. This is because of wear surface softening. At the applied load of 120 N, Ti-6Al-4V, as demonstrated by the arrows in Fig. 12(b), the worn surface had a delamination wear mechanism with deeper scratches over it.

3.5 Corrosion Properties

Figure 13 shows potentiodynamic polarization curves of as-cast Ni-Ti and Ti-6Al-4V alloys in (0.9% NaCl). E_{corr} of Ni-Ti alloy is obviously shifted in the noble direction (≈ -0.34V) compared to the Ti-6Al-4V alloy (≈ -0.49 V). Potentiodynamic curves revealed the presence of a well-defined passive

**Table 3 Corrosion parameters derived from potentiodynamic polarization curves**

	E_{corr}, V	I_{corr}, A/cm^2	Corr. rate, mm/yr	β_a, V/dec	β_c, V/dec
Ni-Ti					
Saline	− 0.496	3.897×10^{-8}	0.00038	0.221	0.171
SBF	− 0.391	3.052×10^{-8}	0.0003	0.238	0.155
Ti-6Al-4V					
Saline	− 0.339	2.497×10^{-8}	0.00017	0.221	0.064
SBF	− 0.412	3.465×10^{-8}	0.00024	0.125	0.074
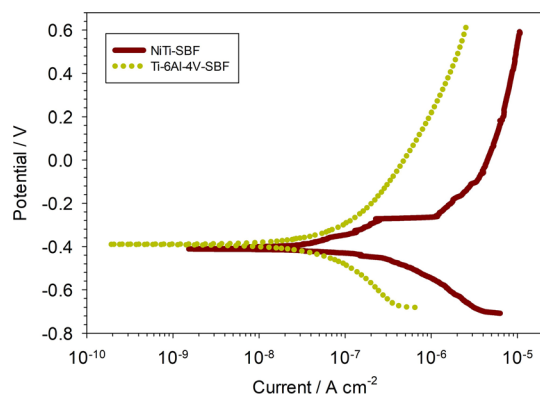
Fig. 14 Potentiodynamic polarization curves of tested alloys in simulated body fluid (SBF)

region for Ti-6Al-4V alloy that extended from − 0.5 to 0.6 V with an average passive current of $\approx 10^{-6}$ A cm^{-2}. On the contrary, Ni-Ti alloy showed a small passive region from − 0.3 to − 0.22 V with an average passive current of 5.0×10^{-7} A cm^{-2}. Above − 0.2 V, the current increased rapidly until a steady value of about 3.0×10^{-5} A cm^{-2}. Potentiodynamic curves are used to calculate corrosion parameters by AutoLab software that are listed in Table 3. The corrosion rate shown by Ti-6Al-4V alloy was 0.000171 mm/yr which was almost half the value obtained for Ni-Ti alloy (0.00038 mm/yr). Potentiodynamic polarization curves were also measured in simulated body fluid (SBF) solution for both Ni-Ti and Ti-6Al-4V samples (Fig. 14). Ti-6Al-4V alloy still shows a well-defined passive region (− 0.4 to 0.6 V) where the current shows a low value lower than 10^{-6} A cm^{-2}. In the case of Ni-Ti alloy, a higher current is shown amounting to 10^{-5} A cm^{-2}; however, this current is low enough to be considered a passive current. On the other hand, both alloys showed almost the same E_{corr} value. The corrosion rate obtained for Ti-6Al-4V alloy (0.00024 mm/yr) was obviously lower than that of Ni-Ti alloy (0.0003 mm/yr), Table 3.

Results of EIS tests in saline solution for Ni-Ti and Ti-6Al-4V alloys are illustrated in Fig. 15 and Table 4. Both Niquest and bode curves revealed that Ti-6Al-4V alloy excelled Ni-Ti alloy. Wider semicircles are shown by the Niquest plot, while the bode curves of Ti-6Al-4V extended to higher impedance values compared to the Ni-Ti alloy. Polarization resistance (R_p) shown by Ti-6Al-4V is quite high (97.1 KΩ) compared to that obtained by the Ni-Ti alloy (37.7 KΩ). Results of EIS testing of both alloys in the SBF solution are shown in Fig. 16 and Table 4. The semicircle shown for Ni-Ti alloy is quite depressed in comparison with the semicircle of Ti-6Al-4V
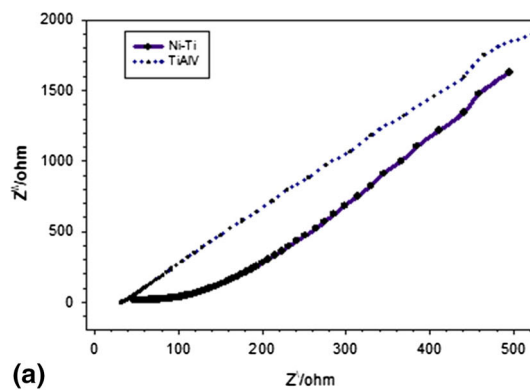
(a)
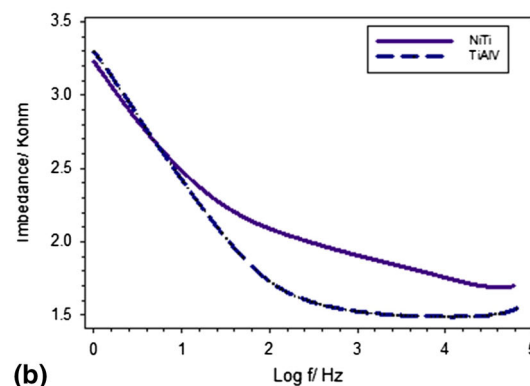
(b)
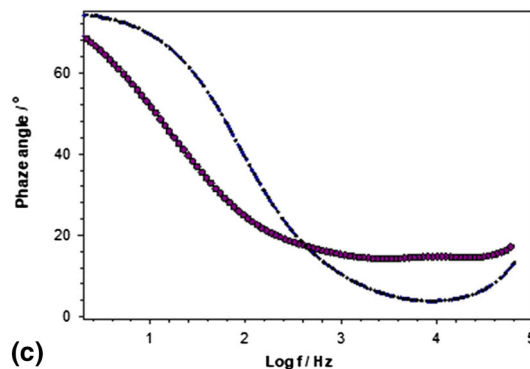
(c)

Fig. 15 Electrochemical impedance curves of tested alloys in saline solution; (a) Niquest (b, c) Bode plot

alloy indicating the high corrosion resistance of the latter. The same trend is substantiated by bode plot where a high impedance value is shown by Ti-6Al-4V compared to Ni-Ti alloy. However, Ti-6Al-4V alloy showed a phase angle as high as 80° compared to 60° for Ni-Ti alloy.

Table 4 EIS results for the investigated as-cast alloys

Alloy	Testing medium	CPE , F	R_p, ohm	R_s, ohm	n
Ti-6Al-4V	Saline	5.45×10^{-6}	2.91×10^5	4.82	0.787
	SBF	4.049×10^{-6}	3.93×10^5	-108	0.787
Ni-Ti	Saline	9.267×10^{-6}	1.717×10^5	19.8	0.770
	SBF	5.016×10^{-6}	3.17×10^5	-223	0.615

Fig. 16 Electrochemical impedance curves of tested alloys in SBF; (a) Niquest; (b,c) Bode plot

Fig. 17 The equivalent circuit for fitting the EIS results

electrical circuit that consists of an active electrolyte resistance R_s in series with the parallel combination of the double-layer capacitance C_{dl} and an impedance of a faradaic electrochemical reaction. It is commonly used in electrochemical impedance spectroscopy (EIS) for the interpretation of impedance spectra, often with a Constant phase element (CPE) replacing the double-layer capacity (C_{dl}).

The effect of saline pH on potentiodynamic polarization curves of Ni-Ti and Ti-6Al-4V alloys was investigated in acidic, neutral, and alkaline media. Figure 18 shows the polarization curves for Ti-6Al-4V alloy at various pH values (3, 7, and 10). The change in pH toward acidic or alkaline values affected negatively the alloy corrosion resistance. In either case, the current was increased, while passivation diminished after a small potential range. Similarly, the change in saline pH exerted a negative effect on Ni-Ti alloy corrosion resistance (Fig. 18). Same as Ti-6Al-4V alloy, the current is increased by changing pH toward acidic or alkaline values.

Corroded samples of both Ni-Ti and Ti-6Al-4V alloys were investigated under FESEM. Figure 19 shows that the investigated samples surfaces are mildly affected and no corrosion damage was observed. However, a mild etched surface of Ni-Ti alloy treated in the saline solution was shown. This sample will be prone to intergranular and pitting corrosion if subjected to a prolonged time of exposure to the saline solution. FESEM observations indicated the high corrosion resistance of Ti-6Al-4V as well as Ni-Ti alloys in SBF and saline solutions.

Corroded surfaces of Ni-Ti and Ti-6Al-4V samples were also examined using the XPS technique which served to analyze and predict the chemical composition of the outermost layer of the surface. XPS spectra of Ni-45Ti alloy (Fig. 20a) revealed a Ti2p3/2 peak corresponding to the presence of TiO_2 while the peak of Ni2p3/2 peak denoted the presence of NiO. However, the quantitative analysis of atomic percentages of both forms indicated that TiO_2 is produced in far greater amounts. Consequently, the alloy surface was covered by titanium oxide with low percentage of nickel oxide. Also, the observed peaks of Ca2p which was formed due to existing of $CaCl_2$ in SBF solution during testing. XPS spectra of Ti-6Al-4V alloy (Fig. 20b) revealed a strong Ti2p3/2 peak correspond-

A simple equivalent circuit (randles circuit) can be used to simulate the EIS behavior as seen in Fig. 17, where R_s is a solution resistance, CPE represents a constant phase element corresponding to the capacitance of the electrode surface, and R_p is a polarization resistance. Randles circuit is an equivalent
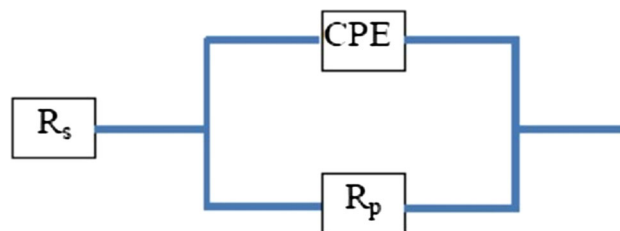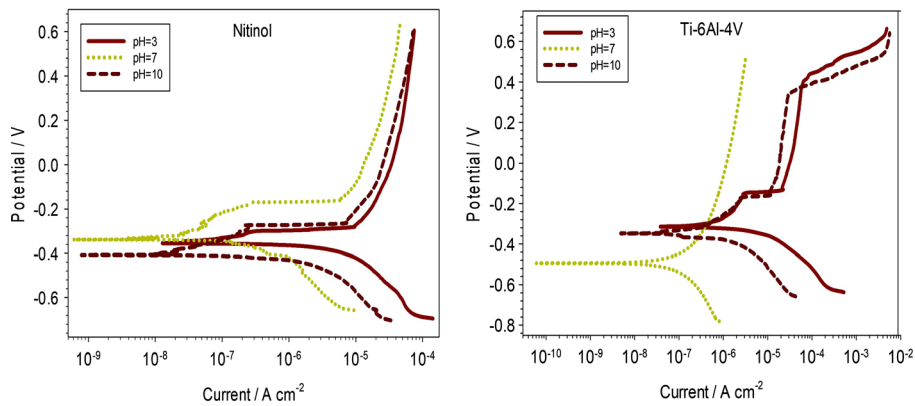
Fig. 18 Potentiodynamic polarization curves of tested alloys at different pH values
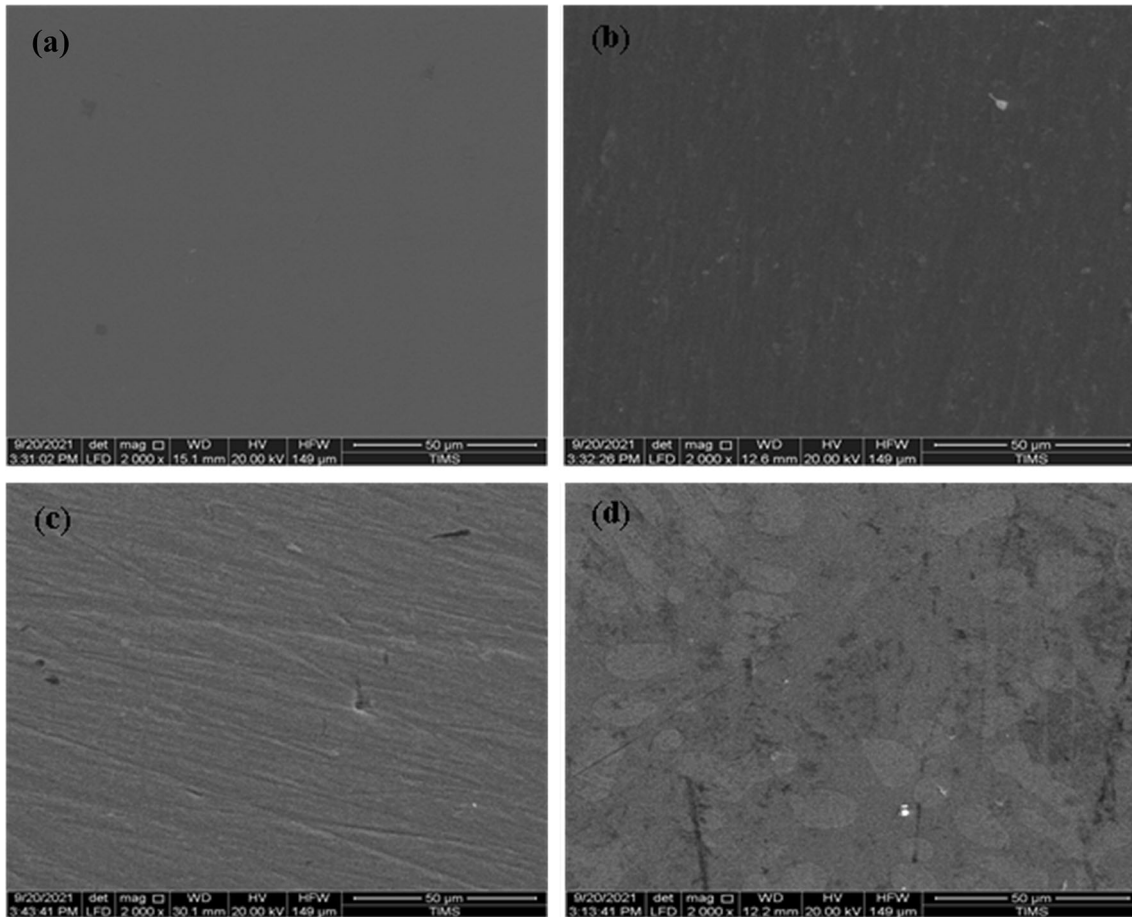

Fig. 19 FESEM of Ni-Ti and Ti-6Al-4V alloys after corrosion testing in SBF; (a) NiTi, (b) Ti64 and in saline solution (c) NiTi, (d) Ti64

ing to the presence of TiO_2. A low intensity peak of Al2p peak denoted also the presence of Al_2O_3. XPS spectra shows also a strong O1s peak of oxygen denoting the presence of titanium and aluminum oxides. The observed peaks of Ca2p and P2p3/2 were formed due to the presence of $CaCl_2$ and NaH_2PO_4 in SBF solution during testing (Ref 49, 50).

According to the obtained results of this study, the corrosion resistance of Ti-6Al-4V alloy excelled that of Ni-Ti alloy, as detailed in the next section. The chemically inert and strongly adhered oxide layer that forms on the metal's surface is responsible for titanium's excellent corrosion resistance in the most aggressive conditions. (Ref 51). The aggressive reaction between Ti and O upon exposure to air or aqueous solutions resulted in oxide film formation with an amorphous or crystalline (rutile or anatase forms) nature. Titanium alloy's corrosion resistance is affected by the toughness of the formed titanium oxide film. The alloying elements in $\alpha + \beta$ and β Ti alloys reduces the corrosion resistance compared to the commercially pure Ti alloys. Titanium alloys possess also high resistance toward microbial corrosion, even in powerful reducing acids because of the spontaneous reformation of the dissolved titanium oxide film.
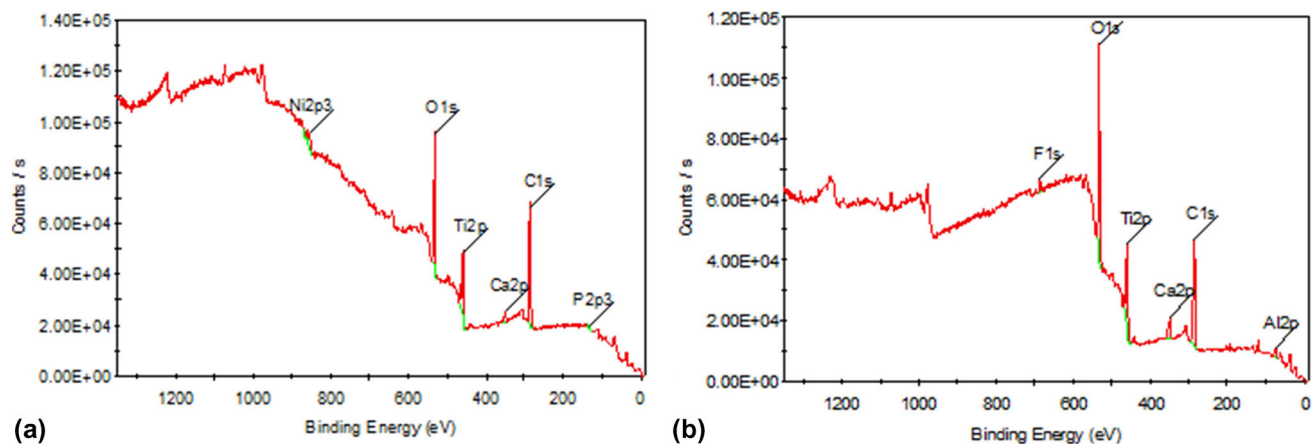
Fig. 20 XPS analysis of (a) Ni-Ti (a) and (b) Ti-6Al-4V alloy surfaces after corrosion testing in SBF solution

In spite of the excellent corrosion resistance of Ti-6Al-4V biomedical alloy, it was observed that Ti, Al, and the V (classified as toxic material) were discharged into the cell tissue due to the dissolution of the passive titanium oxide film and the wear corrosion process (Ref 52). In fact, higher corrosion resistance and less release of the aforementioned ions from Ti6Al4V alloy can be achieved by using TiO$_2$ passive coating on the alloy that is considered strong and more stable. Prosthesis Loosening, fretting corrosion, infection, and metabolism is the common causes of corrosion in the biological bodily fluids of the implanted alloy.

The oxide film formed on Ni-Ti alloy was mainly composed of TiO$_2$; however, Ni as Ni (OH)$_2$ was also detected in a very low percentage ($\approx$ 3.5%) (Ref 50). The increased TiO$_2$ content in the film is expected due to titanium's preferential oxidation. Chemical potentials of Ni (OH)$_2$ and TiO$_2$ at 25 °C, according to conventional chemical potentials ($-$ 108.3 and $-$ 196.3 kcal mol^{-1}, respectively), formation of TiO$_2$ will dominate in comparison to that of Ni (OH)$_2$. In spite of its very low content in the oxide film, in cell tissue fluid, nickel ions were released, which put limitations on using Ni-Ti alloy inside the body.

The presence of Cl$^{-\text{ ions}}$ ions leads to pitting corrosion in Ni-Ti alloy (Ref 53) at higher potentials, because of local dissolution of TiO$_2$ oxide layer in presence of chloride ions. The existence of chloride ions produces a decrease in corrosion potential and an increase in corrosion current, which indicates the depolarization of the anodic reaction. Consequently, the presence of chloride ions enhances the dissolution of titanium oxide as depicted in the following pH-dependent chemical reaction.

$$TiO_2 + 6Cl + 4H^+ \rightarrow TiCl_6^- + 2H_2O$$
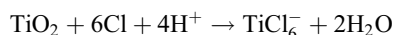
4. Conclusions

The investigated Ni-Ti and Ti-6Al-4V alloys were cast as ingots using **a** vacuum arc melting furnace**.** Hardness, compression, wear rate and corrosion resistance of the as-cast investigated alloys were evaluated. As a result, the following conclusions may be drawn from this study:

1. Microstructure of as-cast Ni-Ti alloy consists of NiTi matrix as well as Ti$_2$Ni dendritic structure. Microstructure of as-cast Ti-6Al-4V alloy structure composed of equiaxed β grains and a variety of α-phase morphologies.

2. Maximum hardness of 446 HV$_{10}$ was reported for Ni-Ti alloy due to existing of Ti$_2$Ni dendrites in the NiTi matrix. Minimum hardness was recorded for Ti-6Al-4V alloy (404 HV$_{10}$) due to the existence of coarse β-grains and inhomogeneity of $\alpha + \beta$ structure.

3. Optimum compressive strength (2042 MPa) and reduction in height (18%) were obtained for Ti-6Al-4V alloy due to existing of a high amount of α-phase in the structure; however, Ni-Ti alloy gave the lowest compressive strength (1804 MPa) and the smallest reduction in height (3%) because of forming Ti$_2$Ni inside NiTi matrix.

4. For dry condition, Ni-Ti alloy showed a relatively lower wear rate compared to Ti-6Al-4V alloy due to existing of Ti$_2$Ni dendrites in the matrix. However, for wet condition, Ti-6Al-4V alloy obtained a significantly lower wear rate than Ni-Ti alloy due to forming a more protective titanium oxide layer.

5. Corrosion rate of Ti-6Al-4V alloy in saline solution (0.9% NaCl) was 0.000171 mm/yr which was almost half of Ni-Ti alloy (0.00038 mm/Yr). The corrosion rate of Ti-6Al-4V in SBF (0.00024 mm/yr) was lower than that of Ni-Ti (0.0003 mm/yr).

6. Results of EIS in saline solution for Ni-Ti and Ti-6Al-4V alloys demonstrated that Ti-6Al-4V alloy excelled Ni-Ti alloy in both Niquest and bode curves. For SBF solution, however, the semicircle of Ni-Ti alloy was very depressed in comparison with the semicircle of Ti-6Al-4V alloy, demonstrating high corrosion resistance of the latter.

7. Corrosion behavior of both Ni-Ti and Ti-6Al-4V alloys is negatively affected by changing pH toward acidic or alkaline values.

8. According to the obtained results for the studied cast alloys, both Ti-6Al-4V and NiTi alloys can be used as orthodontic material because of its low wear rate, low corrosion rate, and high mechanical properties.

Conflict of interest

The authors declare that they have no conflict of interest.

Open Access

References

1. C. Bewerse, L.C. Brinson, and D.C. Dunand, Microstructure and Mechanical Properties of As-Cast Quasibinary NiTi–Nb Eutectic Alloy, *Mater. Sci. Eng. A*, 2015, **627**, p 360–368.
2. S. Jiang and Y. Zhang, Microstructure Evolution and Deformation Behavior of As-Cast NiTi Shape Memory Alloy under Compression, *Trans. Nonferrous Met. Soc. China*, 2012, **22**, p 90–96.
3. K. Ibrahim, N. El-Bagoury, and Y. Fouad, Microstructure and Martensitic Transformation of Cast TiNiSi Shape Memory Alloys, *J. Alloys Compd.*, 2011, **509**, p 3913–3916.
4. K.D. Salman, W.A. Al-Maliki, F. Alobaid, and B. Epple, Microstructural Analysis and Mechanical Characterization of Shape Memory Alloy Ni-Ti-Ag Synthesized by Casting Route, *Appl. Sci.*, 2022, **12**, p 1–10.
5. J. Yeom, J. Kim, J. Hong, S. Kim, C. Park, T. Nam, and K. Lee, Hot Forging Design of As-Cast NiTi Shape Memory Alloy, *Mater. Res. Bull.*, 2014, **58**, p 234–238.
6. E. Montenegro, E. Grassi, J. Simões, P. Sales, and C. Araújo, NiTi Shape Memory Alloy Cellular Meshes: Manufacturing by Investment Casting and Characterization, *Smart Mater. Struct.*, 2020, **29**, p 125008.
7. X. Zhao, L. Ma, Y. Yao, Y. Ding, and X. Shen, Ti_2Ni alloy: A potential Candidate for Hydrogen Storage in Nickel/Metal Hydride Secondary Batteries, *Energy Environ. Sci.*, 2010, **3**, p 1316–1321.
8. F. Geng, P. Shi, and D.Z. Yang, Review on the Development of NiTi Shape Memory Alloy as a Biomaterial, *J. Funct. Mater.*, 2005, **36**, p 11–14.
9. N. El-Bagoury and A. Nofal, Phase Transformation and Microstructure and Mechanical Properties of As Cast NiTiRe Shape Memory Alloys, *Mater. Sci. Technol.*, 2014, **30**(8), p 982–987.
10. K. Li, Y. Liu, X. Liu, X. Wu, S. Zhou, L. Zhang, W. Li, and W. Zhang, Simultaneous Strength-Ductility Enhancement in As-Cast Ti6Al4V Alloy by Trace Ce, *Mater. Des.*, 2022, **215**, p 110491.
11. Z. Zhang, S. Qu, A. Feng, X. Hu, and J. Shen, Microstructural Mechanisms During Multidirectional Isothermal Forging of As-Cast Ti-6Al-4V Alloy with an Initial Lamellar Microstructure, *J. Alloys Compd.*, 2019, **773**, p 277–287.
12. R. Elshaer, M. Abdelhameed, K. Ibrahim, M. El-Shennawy, and A. Sobh, Static and Fatigue Characteristics of Heat-Treated Ti-6Al-3Mo-2Zr-2Sn-2Nb-1.5Cr-0.1Si Alloy, *Metallogr. Microstruct. Anal.*, 2022 https://doi.org/10.1007/s13632-022-00856-9
13. Z. Zhang, S. Qu, A. Feng, X. Hu, and J. Shen, The Low Strain Rate Response of As-Cast Ti-6Al-4V Alloy with an Initial Coarse Lamellar Structure, *Metals*, 2018, **8**(4), p 1–13.
14. S. Oh, K. Woo, S. Kwak, and J. Kim, Effect of Solution Treatment and Short Time Aging on Mechanical Properties of Cast Ti-6Al-4V Alloy, *Korean J. Mater. Res.*, 2016, **26**(5), p 287–291.
15. J. Mathew Donachie Jr., *Titanium: A Technical Guide*, 2nd ed. ASM International, Almere, 2000. (**ISBN 0871706865**)
16. Z.H. Zhang, J. Frenzel, K. Neuking, and G. Eggeler, On the Reaction Between NiTi Melts and Crucible Graphite During Vacuum Induction Melting of NiSi Shape Memory Alloys, *Acta Mater.*, 2005, **53**(14), p 3971–3985.
17. Z.H. Zhang, J. Frenzel, C. Somsen, J. Pesicka, K. Neuking, and G. Eggeler, Orientation Relationship Between TiC Carbides and B2 Phase in As-Cast and Heat-Treated NiTi Shape Memory Alloys, *Mater. Sci. Eng. A*, 2006, **438–440**, p 879–882.
18. O.D. Rigo, J. Otubo, C. Moura, and R. Meip, NiTi SMA Production Using Ceramic Filter During Pouring the Melt, *J. Mater. Process. Technol.*, 2005, **162–163**, p 116–120.
19. S. Jiang, Y. Zhang, and H. Fan, Fracture Behavior and Microstructure of As-Cast NiTi Shape Memory Alloy, *Trans. Nonferrous Met. Soc. China*, 2012, **22**, p 1401–1406.
20. Y. Wen, Y.F. Wang, H. Ran, W. Wei, J.M. Zhang, and C.X. Huang, Improving the Mechanical and Tribological Properties of NiTi Alloys by Combining Cryo-rolling and Post-annealing, *Acta Metall. Sin.*, 2022, **35**, p 317–325.
21. J. Frenzel, P. George, A. Dlouhy, C. Somsen, M.F. Wagner, and G. Egeler, Influence of Ni on Martensitic Phase Transformation in NiTi Shape Memory Alloys, *Acta Mater.*, 2010, **58**(9), p 3444–3458.
22. K. Mehrabi, H. Bahmanpour, A. Shokuhfar, and A. Kneissl, Influence of Chemical Composition and Manufacturing Conditions on Properties of NiTi Shape Memory Alloys, *Mater. Sci. Eng. A*, 2008, **481–482**, p 693–696.
23. S. Seo, H. Choi, G. Lee, K. Lee, J. Han, and M. Jung, Effect of Cooling Rate on Microstructure and Hardness During Solution Treatment and Aging Process of Ti-6Al-4V Alloy for Aerospace Components, *J. Mater. Eng. Perform.*, 2021, **30**, p 3406–3415.
24. S. Liu and Y.C. Shin, Additive Manufacturing of Ti6Al4V Alloy: A Review, *Mater. Des.*, 2019, **164**, p 107552.
25. R.N. Elshaer and K.M. Ibrahim, Effect of Cold Deformation and Heat Treatment on Microstructure and Mechanical Properties of TC21 Ti-Alloy, *Trans. Nonferrous Met. Soc. China*, 2020, **30**, p 1290–1299.
26. I.V. Okulov, S. Pauly, U. Kühn, P. Gargarella, T. Marr, J. Freudenberger, L. Schultz, J. Scharnwebere, C.-G. Oertel, W. Skrotzki, and J. Eckert, Effect of Microstructure on the Mechanical Properties of Ascast Ti–Nb–Al–Cu–Ni Alloys for Biomedical Application, *Mater. Sci. Eng. C*, 2013, **33**, p 4795–4801.
27. J. Chen, L. Xue, M. King, and G. Campbell, High Power CW YAG Laser Weldability of Dissimilar Ti to Ni Metal Plates through Beam Shift, *Int. J. Adv. Manuf. Technol.*, 2019, **104**, p 489–501.
28. K. Ibrahim, A. Hussien, and M. Abdelkawy, Effect of Si-Addition as a Grain Refiner on Microstructure and Properties of Ti-6Al-4V Alloy, *Trans. Nonferrous Met. Soc. China*, 2013, **23**, p 1863–1874.
29. R.N. Elshaer, M.S. El-Deeb, S.S. Mohamed, and K.M. Ibrahim, Effect of Strain Hardening and Aging Processes on Microstructure Evaluation, Tensile and Fatigue Properties of Cast Ti-6Al-2Zr-2Sn-2Mo-1.5Cr-2Nb-0.1Si Alloy, *Int. J. Metalcast.*, 2022, **16**(2), p 723–737.
30. I. Damisih, I.N. Jujur, J. Sah, and D.H. Prajitno, Effect of Heat Treatment Temperature on Microstructure Characteristic and Hardness Properties of Casted Ti-6Al-4V ELI, *Widyariset*, 2018, **4**(2), p 153–162.
31. S. Singh, A.N. Jinoop, I.A. Palani, C.P. Paul, K.P. Tomar, and K.G. Prashanth, Microstructure and Mechanical Properties of NiTi-SS Bimetallic Structures Built Using Wire Arc Additive Manufacturing, *Mater. Lett.*, 2021, **303**, p 130499.
32. K.M. Ibrahim, A.M. El-Hakeem, and R.N. Elshaer, Microstructure and Mechanical Properties of Cast and Heat treated Ti−6.55Al−3.41Mo−1.77Zr Alloy, *Trans. Nonferrous Met. Soc. China*, 2013, **23**, p 3517–3524.
33. P.Y. Li, Y.S. Wang, F.Y. Meng, L. Cao, and Z.R. He, Effect of Heat Treatment Temperature on Martensitic Transformation and Superelasticity of the $Ti_{49}Ni_{51}$ Shape Memory Alloy, *Materials*, 2019, **12**, p 2539.

34. A. Ahadi, T. Kawasaki, S. Harjo, W.S. Ko, Q.P. Sun, and K. Tsuchiya, Reversible Elastocaloric Effect at Ultra-low Temperatures in Nanocrystalline Shape Memory Alloys, *Acta Mater.*, 2019, **165**, p 109–117.

35. Q.P. Sun, A. Ahadi, M.P. Li, and M.X. Chen, Effects of Grain Size on Phase Transition Behavior of Nanocrystalline Shape Memory Alloys, *Sci. China Technol. Sci.*, 2014, **57**, p 671–679.

36. A. Ahadi and Q.P. Sun, Stress Hysteresis and Temperature Dependence of Phase Transition Stress in Nanostructured NiTi-Effects of Grain Size, *Appl. Phys. Lett.*, 2013, **103**, p 021902.

37. P. Li, Y. Jia, Y. Wang, Q. Li, F. Meng, and Z. He, Effect of Fe Addition on Microstructure and Mechanical Properties of As-Cast $Ti_{49}Ni_{51}$ Alloy, *Materials*, 2019, **12**, p 1–15.

38. A. Molinari, G. Straffelini, B. Tesi, and T. Baccai, Dry Sliding Wear Mechanism of the Ti6Al4V Alloy, *Wear*, 1997, **208**, p 105–112.

39. S. Singh, S. Gangwar, and S. Yadav, A Review on Mechanical and Tribological Properties of Micro/Nano Filled Metal Alloy Composites, *Mater. Today Proc.*, 2017, **4**, p 5583–5592.

40. V. Mortazavi and M. Khonsari, On the Prediction of Transient Wear, *J. Tribol-Trans. ASME*, 2016, **138**, p 041604.

41. D.S. Prasad and C. Shoba, Hybrid Composites—A Better Choice for High Wear Resistant Materials, *J. Mater. Res. Technol.*, 2014, **3**, p 172–178.

42. X.L. Li, X.C. Chen, C.H. Zhang, and J.B. Luo, Preparation of Self-Lubricating NiTi Alloy and Its Self-Adaptive Behavior, *Tribol. Int.*, 2019, **130**, p 43–51.

43. P. Šittnera, P. Sedlákb, H. Seiner, P. Sedmák, J. Pilcha, R. Delville, L. Heller, and L. Kadeřávek, On the Coupling between Martensitic Transformation and Plasticity in NiTi: Experiments and Continuum based Modelling, *Prog. Mater. Sci.*, 2018, **98**, p 249–298.

44. Y. Wang, R. Xu, S. Hu, F. Tu, and W. Jin, Research Combining Experiment and FEM Analysis on Sliding Wear Behaviors and Mechanisms of TiNi Alloy, *Wear*, 2017, **386**, p 218–222.

45. A.A. Misochenko, S.V. Chertovskikh, L.S. Shuster, and V.V. Stolyarov, Influence of Grain Size and Contact Temperature on the Tribological Behaviour of Shape Memory $Ti_{49.3}Ni_{50.7}$ Alloy, *Tribol. Lett.*, 2017, **65**, p 1–7.

46. M. Mehdi, K. Farokhzadeh, and A. Edrisy, Dry Sliding Wear Behavior of Superelastic Ti–10V–2Fe–3Al β-Titanium Alloy, *Wear*, 2016, **350**, p 10–20.

47. O. Alam and A. Haseeb, Response of Ti-6Al-4V and Ti-24Al-11Nb Alloys to Dry Sliding Wear Against Hardened Steel, *Tribol. Int.*, 2002, **35**(6), p 357–362.

48. W. Zhang, S. Yamashita, and H. Kita, Effects of Load on Tribological Properties of B_4C and B_6C-SiC Ceramics Sliding Against SiC Balls, *Mater. Des.*, 2020, **190**, p 586–596.

49. NIST X-ray Photoelectron Spectroscopy Database, NIST Standard Reference Database 20, Version 4.1. https://doi.org/10.18434/T4T88K

50. N. Figueira, T.M. Silva, M.J. Carmezim, and J.C.S. Fernandes, Corrosion Behaviour of NiTi Alloy, *Electrochim. Acta*, 2009, **54**, p 921–926.

51. M.O. Bodunrin, L.H. Chown, J.W. van der Merwe, K.K. Alaneme, C. Oganbule, D.E. Klenam, and N.P. Mphasha, Corrosion Behavior of Titanium Alloys in Acidic and Saline Media: Role of Alloy Design, Passivation Integrity, and Electrolyte Modification, *Corros. Rev.*, 2020, **38**, p 1–20.

52. R.W. Hsua, C.C. Yang, C.A. Huang, and Y. Chen, Investigation on the Corrosion Behavior of Ti-6Al-4V Implant Alloy by Electrochemical Techniques, *Mater. Chem. Phys.*, 2004, **86**, p 269–278.

53. M. Mirjalili, M. Momeni, N. Ebrahimi, and M.H. Moayed, Comparative Study on Corrosion Behavior of Nitinol and Stainless-Steel Orthodontic Wires in Simulated Saliva Solution in Presence of Fluoride Ions, *Mater. Sci. Eng. C*, 2013, **33**, p 2084–2093.